SUPPORTING INFORMATION

Band energy diagram calculations.

Optical band gap energies (E_g) were obtained from Tauc plots, were the Kubelka-Munk function, $(F(R)h\nu)^{1/n}$, is plotted against the energy. The value of *n* depends on the nature of the transitions within the semiconductor electronic structure, being $n = 2$ for indirect allowed transitions in the case of the materials under study. Work function (φ) of each of the studied samples, which determines the position of its respective Fermi level (E_F) with respect to the vacuum (E_{vac}), is extrapolated from the UPS measurements (shown in Fig. S9a). Interpolation of the onset energy (E_{HOMO}) obtained from the low-energy tail of the UPS spectrum is the difference between the Fermi level and the valence band maximum energy (E_{VBM}). This way, E_{VBM} can be calculated using equation (1). Knowing the E_{VBM} and the optical band gap, the conduction band minimum energy (E_{CBM}) can be estimated from equation (2):

$$E_{VBM}\ (vs. E_{vac}) = -E_{HOMO} - E_F \qquad (1)$$

$$E_{CBM}\ (vs. E_{vac}) = E_{VBM} + E_g \qquad (2)$$

To compare the bands energies of the materials with the reduction potential of CO_2 to the generated products and water oxidation potential, obtained band energy values were converted to vs. NHE scale using equation (3):

$$E_{vs.\ NHE} = -E_{vs.\ vac} - 4.44 \qquad (3)$$

Apparent Quantum Yield calculations.

A. Q. Y. for the main photocatalysts under study were calculated using equation (4):

$$A.Q.Y. = \frac{number\ of\ transferred\ electrons}{number\ of\ photons} = \frac{8\times molecules\ of\ CH_4 + 2\times molecules\ of\ CO + 2\times molecules\ of\ H_2}{\frac{I\cdot A\cdot t}{hc/\lambda}} \qquad (4)$$

Where *I*, *A*, *t*, *h*, *c* and *λ*, are referred to the intensity of the incident light, the area of irradiation, the time of irradiation, Planck's constant, speed of light in the vacuum and wavelength of incident light, respectively. The number of molecules of each product was obtained by multiplying the produced amount in mol by $6.022\cdot10^{23}$.

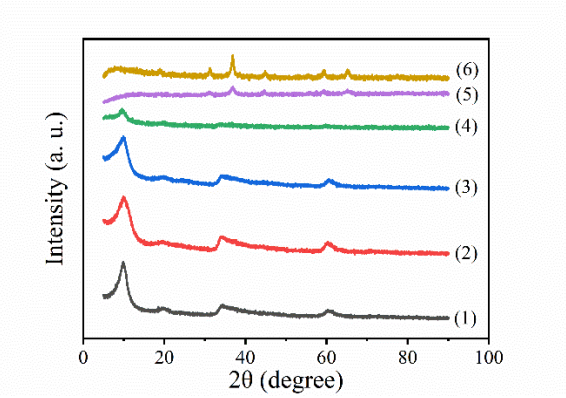

Figure S1. XRD patterns of NiL41 (1), NiL420 (2), NiL210 (3), CoL210 (4), CoM21 (5) and CoM410 (6).

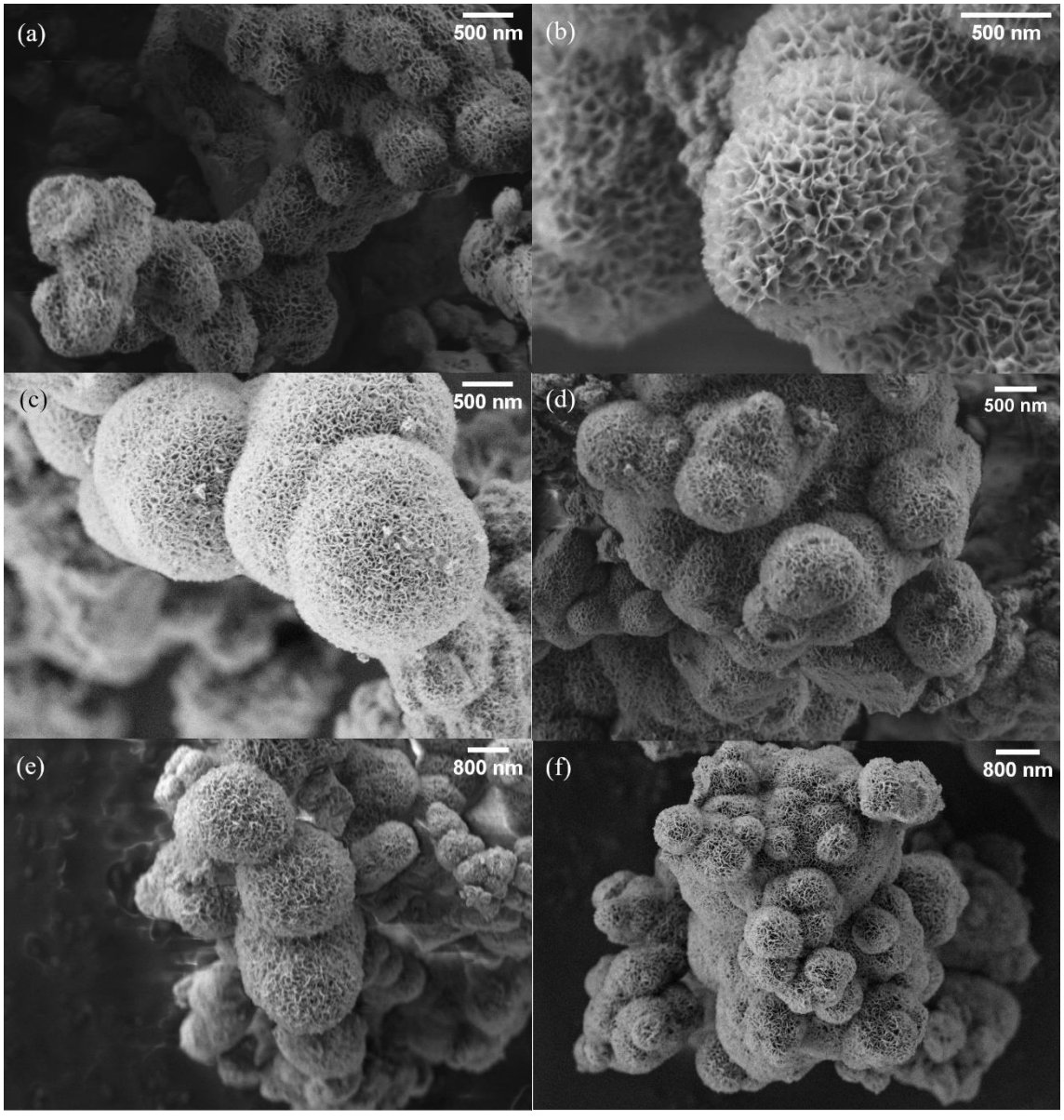

Figure S2. FESEM images of NiL41 (a), NiL410 (b), NiL420 (c), NiL210 (d), CoL21 (e) and CoL210 (f). Influence of precursor concentration on the morphology can be inferred from the comparison in Figures S2a-c.

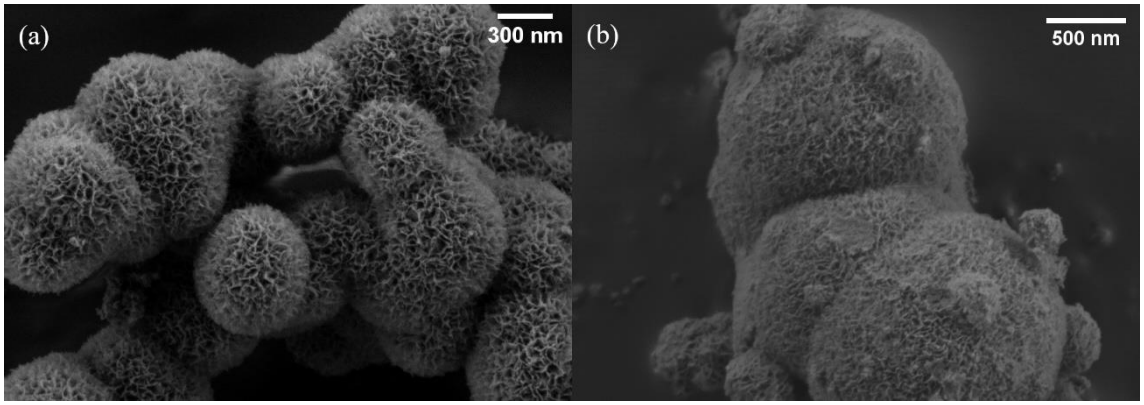

Figure S3. FESEM images of NiM410 (a), and CoM21 (b). Concentration of precursors in the synthesis also influences the morphology, as seen in pristine LDH. Morphology is retained upon calcination.

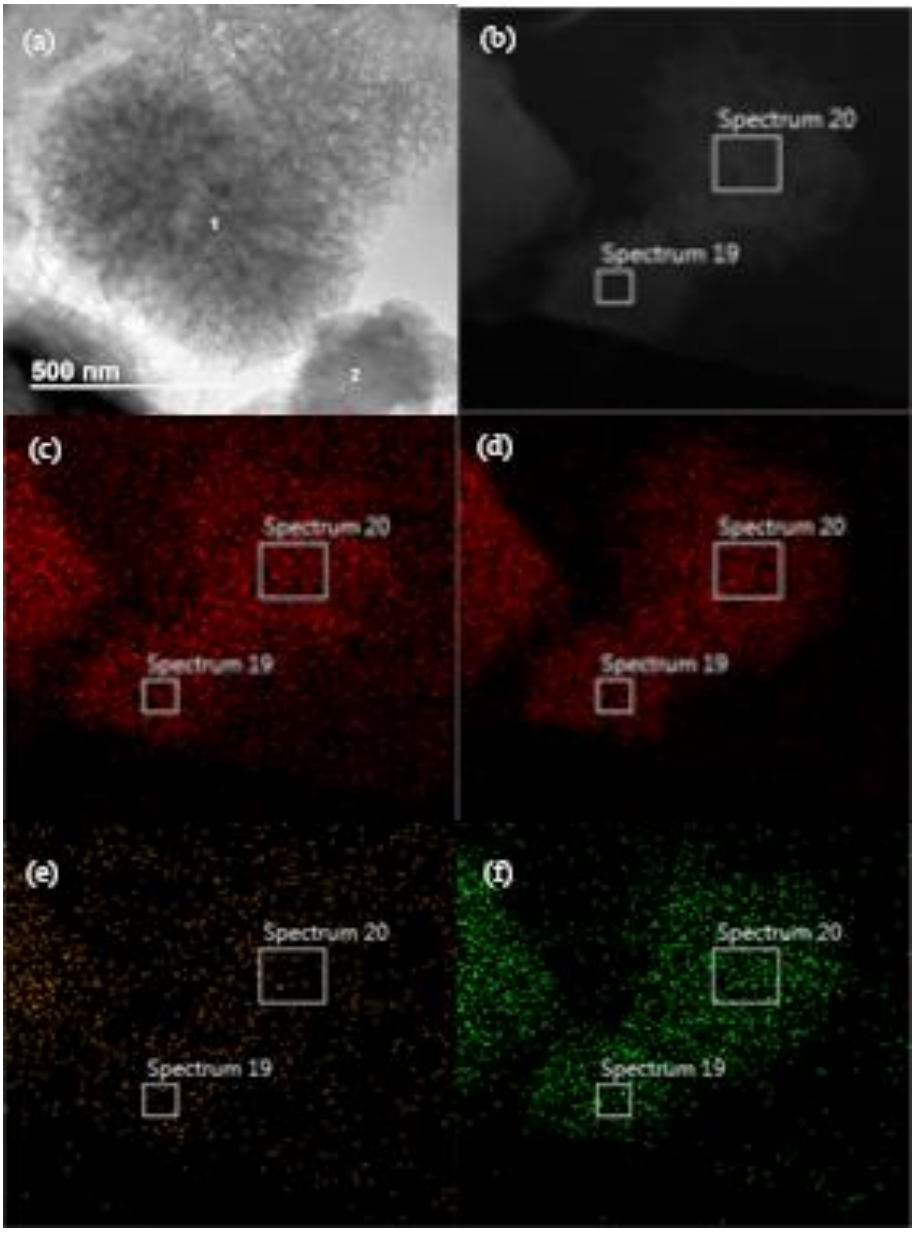

Figure S4. TEM cross-section image of CoL21 spherical particles in which no residual Ti-rich core remains (1) and showing still a residual Ti-rich core (2). Elemental mapping based on STEM image of CoL21 lamellar cross-section showing the obtained STEM image (b), and O (c), Co (d), Ti (e) and Al (f) element distribution.

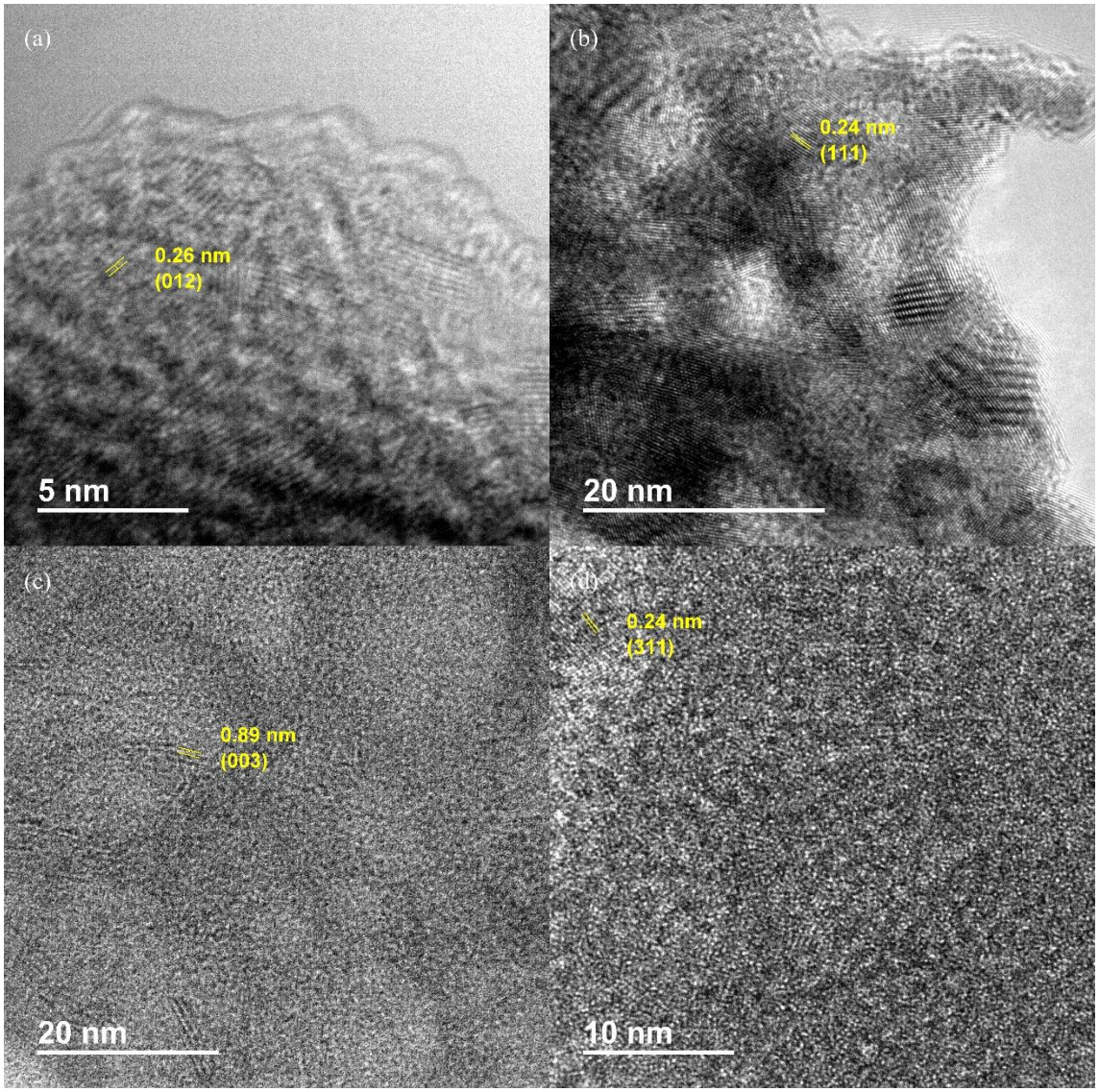

Figure S5. HRTEM images and representative lattice spacings for NiL410 (a), NiM410 (b), CoL21 (c) and CoM210 (d).

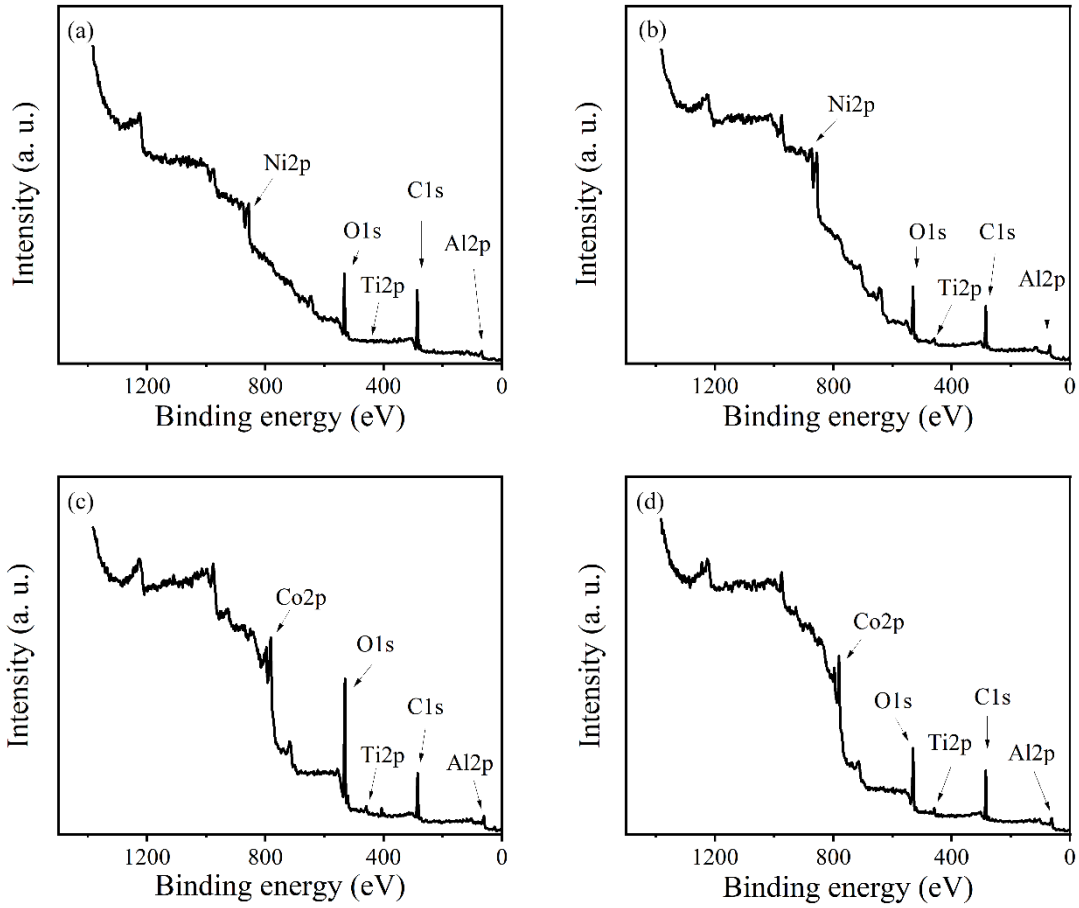

Figure S6. Survey XP spectra of NiL410 (a), NiM410 (b), CoL21 (c) and CoM210 (d).

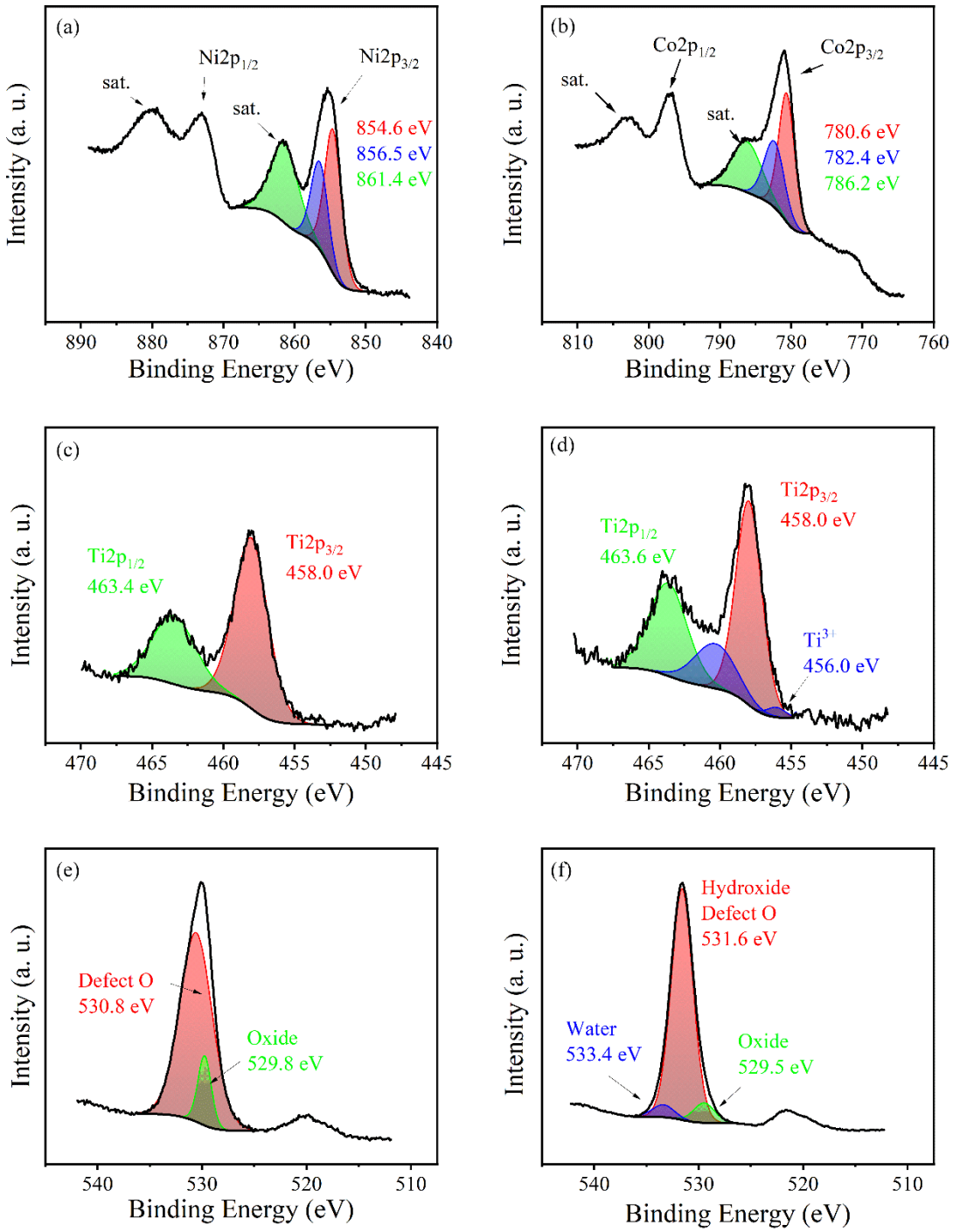

Figure S7. High resolution XPS of Ni 2p peak in NiM410 (a); Co 2p peak in CoL21 (b); Ti 2p peak in NiM410 (c) and CoL21 (d); O 1s peak in NiM410 (e) and CoL21 (f).

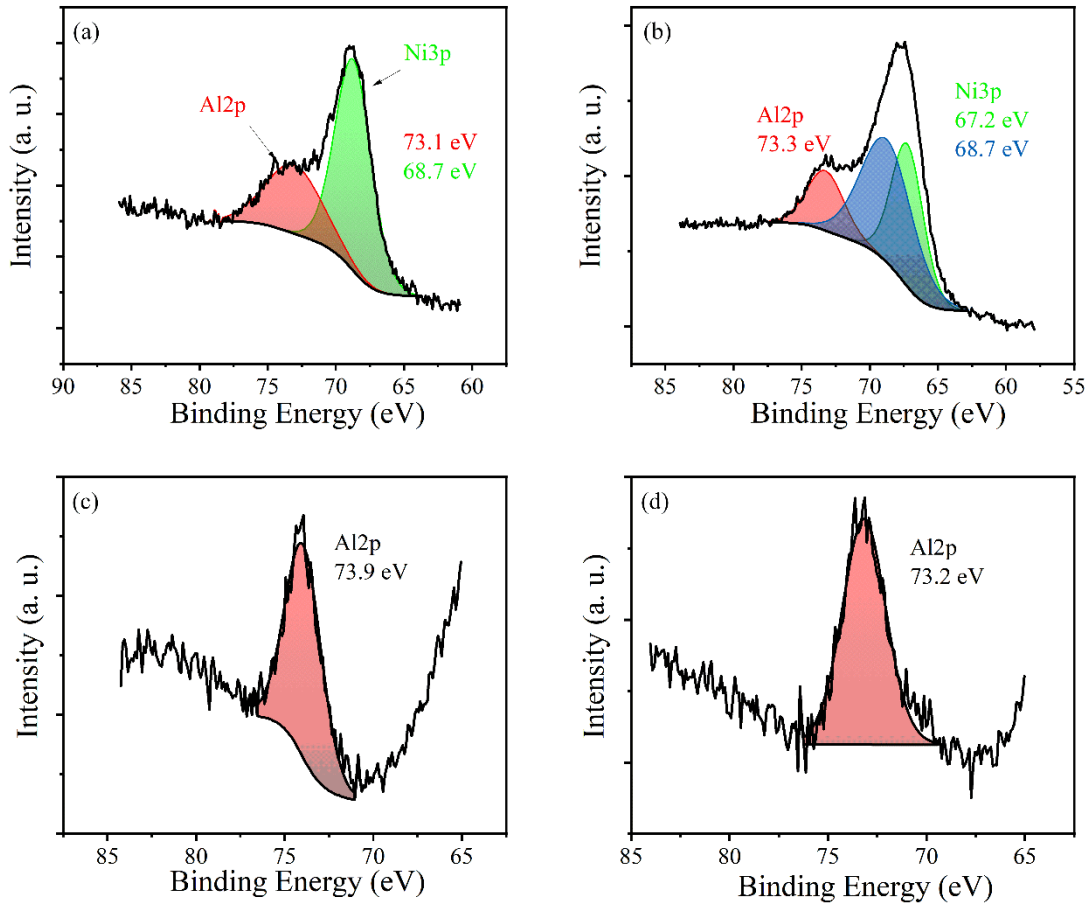

Figure S8. High resolution XPS of Al 2p peak in NiL410 (a), NiM410 (b), CoL21 (c) and CoM210 (d).

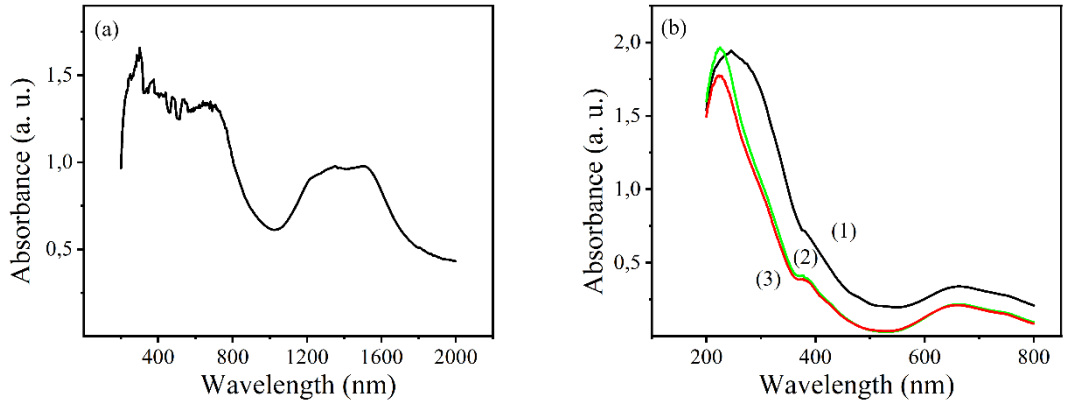

Figure S9. Diffuse reflectance UV-Vis-NIR absorption spectra of CoM210 (a). Diffuse reflectance UV-Vis absorption spectra of Ni-based LDH at different precursor concentrations (b): NiL41 (1), NiL410 (2) and NiL420 (3).

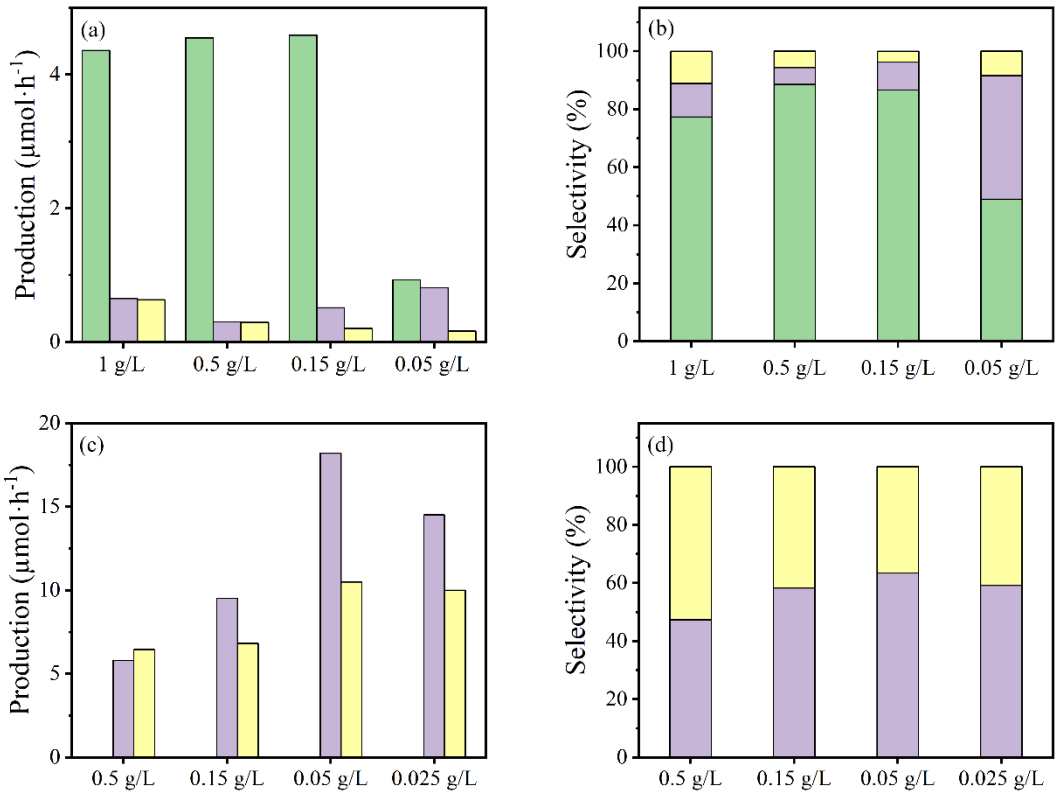

Figure S10. Production and selectivity for CO_2 photoreduction at different catalyst concentrations for NiL410 (a-b) and CoM210 (c-d). Products generated are CH_4 (green), CO (purple) and H_2 (yellow). Reaction conditions: 20 ml of CH_3CN:H_2O:TEOA 3:1:1 solution, different amounts of photocatalyst, 6.6 mg $Ru(bpy)_3Cl_2$, T: 50 ºC, solar simulator light (AM 1.5G filter, 100 mW/cm^2).

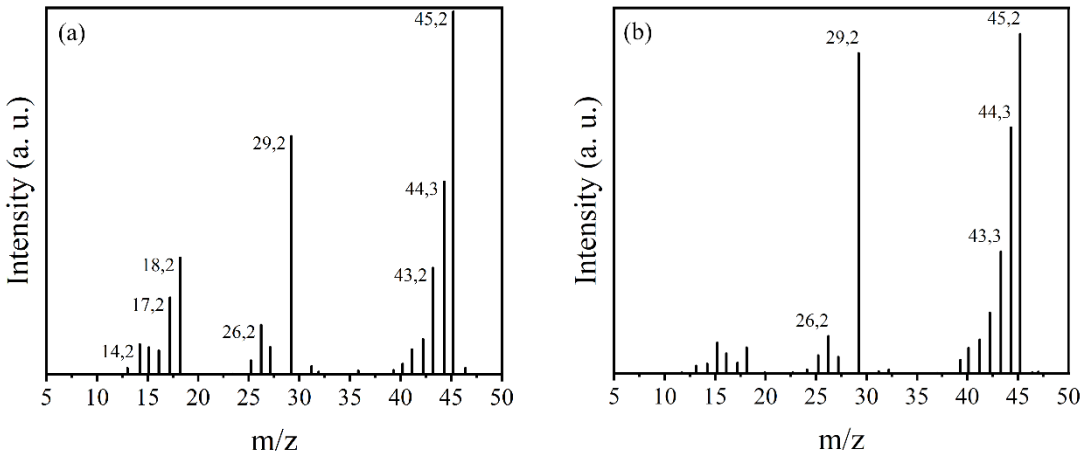

Figure S11. Mass spectrometry spectra for $^{13}CO_2$ photoreduction over NiL410 (a) and CoM210 (b). Reaction conditions: 20 ml of CH_3CN:H_2O:TEOA 3:1:1 solution, 3 mg (NiL410) or 1 mg (CoM210) of photocatalyst, 6.6 mg $Ru(bpy)_3Cl_2$, T: 50 ºC, solar simulator light (AM 1.5G filter, 100 mW/cm^2).

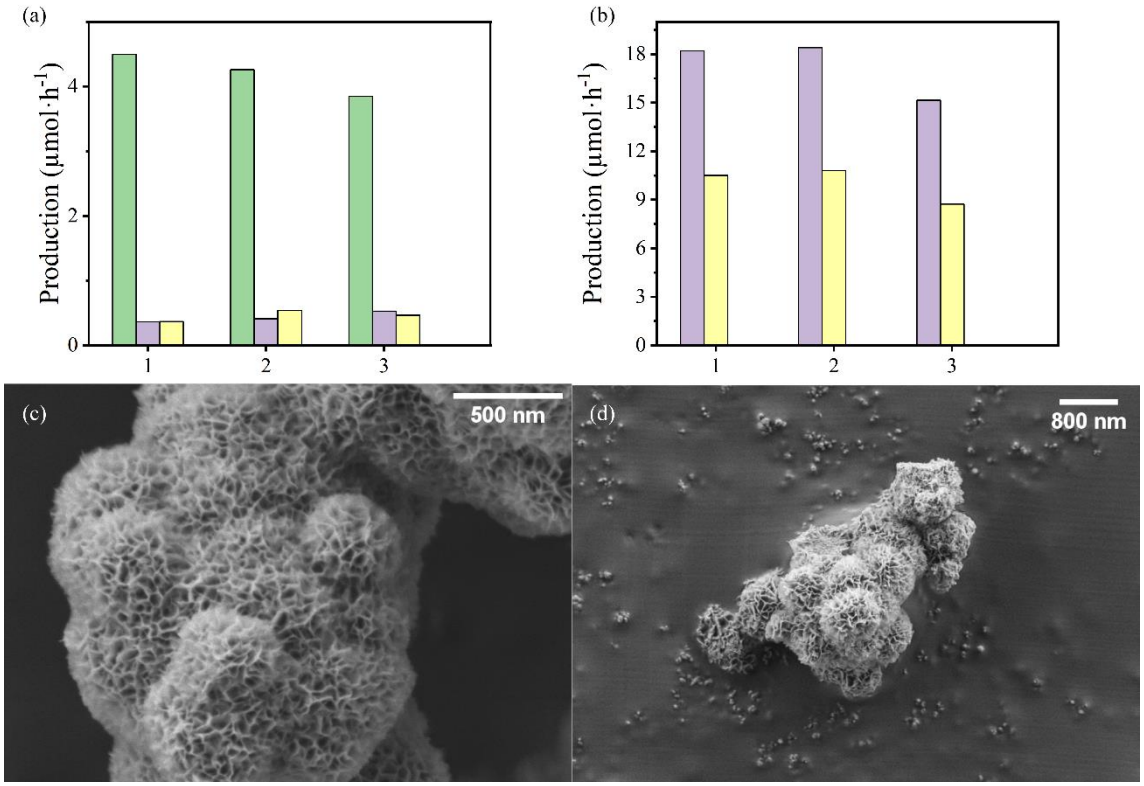

Figure S12. CO_2 photoreduction production upon consecutive uses for NiL410 (a) and CoM210 (b). Products generated are CH_4 (green), CO (purple), and H_2 (yellow). Reaction conditions: 20 ml of CH_3CN:H_2O:TEOA 3:1:1 solution, 10 mg of photocatalyst, 6.6 mg $Ru(bpy)_3Cl_2$, T: 50 ºC, solar simulator light (AM 1.5G filter, 100 mW/cm^2). FESEM images of NiL410 (c) and CoMO210 (d) recovered after the third photocatalytic test.

Table S1. Summary of the state of the art for photocatalytic CO_2 reduction to form CH_4 using $Ru(bpy)_3^{2+}$ as photosensitizer upon solar or visible light irradiation.

MATERIAL	CH_4 prod. (µmol/h)	Selectivity (%)	A. Q. Y. (%)[a]	CONDITIONS	**Ref.**
NiCo-LDH hollow nanocages	2.8	62.7	No data	300 W Xe lamp >400nm Catalyst (0.5 mg/ml) $Ru(bpy)_3Cl_2$ (0.33 mg/ml) ACN:H_2O:TEOA, CO_2 1.8 bar	[1]
Ultrathin NiMn-LDH	1.6	92.3	0.32 (550 nm)	300 W Xe lamp >400nm Catalyst (1 mg/ml) $Ru(bpy)_3Cl_2$ (0.33 mg/ml) ACN:H_2O:TEOA, CO_2 1.8 bar	[2]
NiVAl-LDH	2.17	78.9	No data	300 W Xe lamp >400 nm Catalyst (1 mg/ml) $Ru(bpy)_3Cl_2$ (0.33 mg/ml) ACN:H_2O:TEOA, CO_2 1.8 bar	[3]
Ultrathin NiAl-LDH	1.03	70.3	4.13 (470 nm)	300 W Xe lamp >400 nm (1150 $mW \cdot cm^{-2}$) Catalyst (1 mg/ml) $Ru(bpy)_3Cl_2$ (0.33 mg/ml)	[4]

				ACN:H_2O:TEOA, CO_2 1.8 bar	
Ultrathin NiFe-LDH	1.53	81.8	No data	300 W Xe lamp >400 nm Catalyst (1 mg/ml) $Ru(bpy)_3Cl_2$ (0.33 mg/ml) ACN:H_2O:TEOA, CO_2 1.8 bar	[5]
NiTiAl-LDH	2.96	86	No data	Solar AM 1.5G (100 mW·cm^{-2}) Catalyst (1 mg/ml) $Ru(bpy)_3Cl_2$ (0.33 mg/ml) ACN:H_2O:TEOA, CO_2 0.5 bar	[6]
$ZnFeO_4/TiO_2/CoO_x$/Au-Cu	0.21	93.8	2.14 (420 nm)	Solar AM 1.5G (100 mW·cm^{-2}) Catalyst (10 mg) H_2O (0.5 ml) CO_2 ambient pressure	[7]
NiLDH410	4.59	86.6	1.95 (405 nm)	Solar AM 1.5G (100 mW·cm^{-2}) Catalyst (0.15 mg/ml) $Ru(bpy)_3Cl_2$ (0.33 mg/ml) ACN:H_2O:TEOA, CO_2 0.5 bar	**This Work**

[a]A. Q. Y. means apparent quantum yields.

Table S2. Summary of the state of the art for photocatalytic CO_2 reduction to form CO using $Ru(bpy)_3^{2+}$ as photosensitizer upon solar or visible light irradiation.

MATERIAL	CO prod. (μmol/h)	Selectivity (%)	A. Q. Y. (%)[a]	CONDITIONS	Ref.
Hollow ZnCo-LDH	134.2	76.9	6.76 (450 nm)	300 W Xe lamp >420 nm Catalyst (0.01 mg/ml) $Ru(bpy)_3Cl_2$ (1 mg/ml) ACN:H_2O:TEOA, CO_2 1 bar	[8]
Cu_2S/ROH-$NiCo_2O_3$	21.3	72	1.01 (400 nm)	300 W Xe lamp >400 nm Catalyst (0.125 mg/ml) $Ru(bpy)_3Cl_2$ (0.4 mg/ml) ACN:H_2O:TEOA, CO_2 1 bar	[9]
Ni-Co_3O_4	44.3	Variable	3.7 (450 nm)	300 W Xe lamp >420 nm (872 $W \cdot m^{-2}$) Catalyst (0.03 mg/ml) $Ru(bpy)_3Cl_2$ (1.67 mg/ml) ACN:H_2O:TEOA, CO_2 1 bar	[10]
$Ni(OH)_2$/Graphene	10.7	96	1.03 (450 nm)	300 W Xe lamp >420 nm (405 $mW \cdot cm^{-2}$) Catalyst (0.17 mg/ml)	[11]

				$Ru(bpy)_3Cl_2$ (1.25 mg/ml) ACN:H_2O:TEOA, no PCO_2 data	
$Ni(OH)_2$ nanocages	43.2	96.1	2.50 (420 nm)	100 W LED lamp, 420 nm Catalyst (0.03 mg/ml) $Ru(bpy)_3Cl_2$ (0.9 mg/ml) ACN:H_2O:TEOA, CO_2 0.8 bar	[12]
Ultrathin CoAl-LDH	25.2	60.9	0.92 (420 nm)	300 W Xe lamp (400-800 nm, 500 $mW \cdot cm^{-2}$) Catalyst (1 mg/ml) $Ru(bpy)_3Cl_2$ (0.33 mg/ml) ACN:H_2O:TEOA, CO_2 1.8 bar	[13]
NiO/Co_3O_4	16.15	71	No data	300 W Xe lamp >420 nm (1.2 W) Catalyst (0.17 mg/ml) $Ru(bpy)_3Cl_2$ (1.33 mg/ml) ACN:H_2O:TEOA, no PCO_2 data	[14]

Mxene/CoCo-LDH	6.3	63.9	0.92 (420 nm)	5 W LED lamp (400-1000 nm) Catalyst (0.08 mg/ml) $Ru(bpy)_3Cl_2$ (1.25 mg/ml) ACN:H_2O:TEOA, no PCO_2 data	[15]
CoMO210	15.14	63.4	1.12 (405 nm)	Solar 1.5 AMG (100 $mW \cdot cm^{-2}$) Catalyst (0.05 mg/ml) $Ru(bpy)_3Cl_2$ (0.33 mg/ml) ACN:H_2O:TEOA, CO_2 0.5 bar	**This Work**

[a]A. Q. Y. means apparent quantum yields.

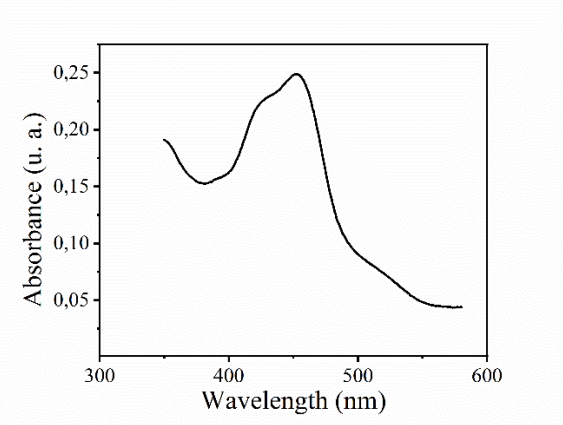

Figure S13. UV-vis absorption spectrum of a $Ru(bpy)_3Cl_2$ water solution (1 mg/ml).

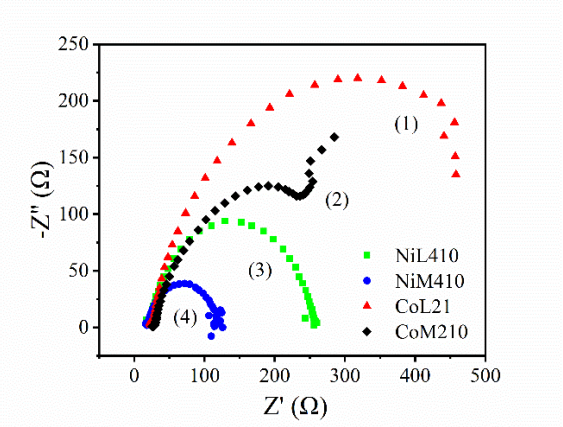

Figure S14. Nyquist plots of the best performing samples under study as indicated in the graph. Electrolyte: 0.1 M Na_2SO_4 in water. Electrochemical cell: LDH/FTO working electrode, Ag/AgCl reference electrode and Pt counter electrode. Atmosphere: N_2. Scanning frequency range: 0.01 Hz-100 kHz at 1 V vs Ag/AgCl.

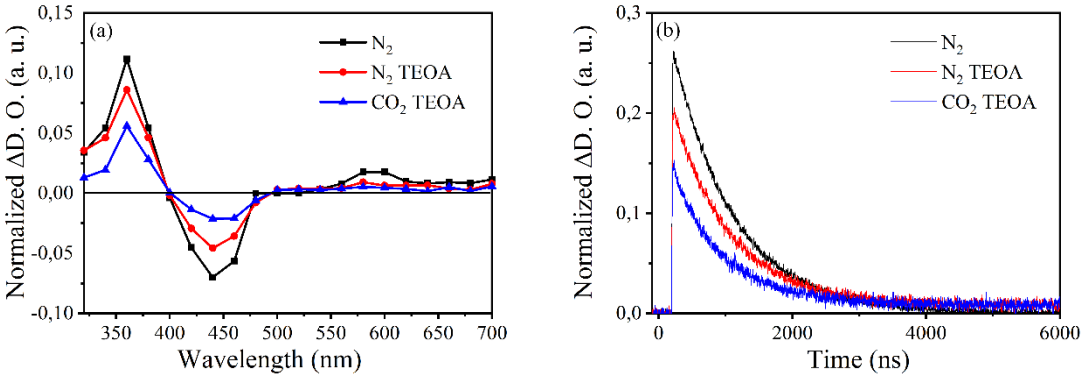

Figure S15. Transient absorption spectrum of $Ru(bpy)_3Cl_2$ (a) recorded at 1 μs acquisition time with an excitation wavelength of 450 nm. Transient signal decays (b) monitored at 360 nm after 450 nm laser flash in the absence or presence of TEOA and TEOA and CO_2.

References

1. X. Hao, L. Tan, Y. Xu, Z. Wang, X. Wang, S. Bai, C. Ning, J. Zhao, Y. Zhao, Y. Song, Engineering Active Ni Sites in Ternary Layered Double Hydroxide Nanosheets for a Highly Selective Photoreduction of CO2 to CH4 under Irradiation above 500 nm, Ind Eng Chem Res 59 (2020) 3008-3015. https://doi.org/10.1021/acs.iecr.9b06464.

2. L. Tan, S. Xu, Z. Wang, X. Hao, T. Li, H. Yan, W. Zhang, Y. Zhao, Y. Song, 600 nm induced nearly 99% selectivity of CH4 from CO2 photoreduction using defect-rich monolayer structures, Cell Reports Physical Science 2 (2021) 100322. https://doi.org/10.1016/j.xcrp.2021.100322.

3. S. Yu, L. Tan, S. Bai, C. Ning, G. Liu, H. Wang, B. Liu, Y. Zhao, Y. Song, Rational Regulation of Electronic Structure in Layered Double Hydroxide Via Vanadium Incorporation to Trigger Highly Selective CO2 Photoreduction to CH4, Small 18 (2022) 2202334. https://doi.org/10.1002/smll.202202334.

4. L. Tan, S. Xu, Z. Wang, Y. Xu, X. Wang, X. Hao, S. Bai, C. Ning, Y. Wang, W. Zhang, Y.K. Jo, S. Hwang, X. Cao, X. Zheng, H. Yan, Y. Zhao, H. Duan, Y. Song, Highly Selective Photoreduction of CO2 with Suppressing H2 Evolution over Monolayer Layered Double Hydroxide under Irradiation above 600 nm, Angew. Chem. Int. Ed. 58 (2019) 11860-11867. https://doi.org/10.1002/anie.201904246.

5. S. Bai, T. Li, H. Wang, L. Tan, Y. Zhao, Y. Song, Scale-up synthesis of monolayer layered double hydroxide nanosheets via separate nucleation and aging steps method for efficient CO2 photoreduction, Chem. Eng. J. 419 (2021) 129390. https://doi.org/10.1016/j.cej.2021.129390.

6. M. Molina-Muriel, Y. Peng, H. García, A. Ribera, Increased photocatalytic activity and selectivity towards methane of trimetallic NiTiAl-LDH, J. Alloys Compounds 897 (2022) 163124. https://doi.org/10.1016/j.jallcom.2021.163124.

7. X. Liu, Y. Chen, Q. Wang, L. Li, L. Du, G. Tian, Improved charge separation and carbon dioxide photoreduction performance of surface oxygen vacancy-enriched zinc ferrite@titanium dioxide hollow nanospheres with spatially separated cocatalysts, J. Colloid Interface Sci. 599 (2021) 1-11. https://doi.org/10.1016/j.jcis.2021.04.104.

8. F. Wang, R. Fang, X. Zhao, X. Kong, T. Hou, K. Shen, Y. Li, Ultrathin Nanosheet Assembled Multishelled Superstructures for Photocatalytic CO2 Reduction, ACS Nano 16 (2022) 4517-4527. https://doi.org/10.1021/acsnano.1c10958.

9. L. Li, X. Dai, D. Chen, Y. Zeng, Y. Hu, X.W.(. Lou, Steering Catalytic Activity and Selectivity of CO2 Photoreduction to Syngas with Hydroxy-Rich Cu2S@ROH-NiCo2O3 Double-Shelled Nanoboxes, Angew. Chem. Int. Ed. 61 (2022) e202205839. https://doi.org/10.1002/anie.202205839.

10. G. Qian, W. Lyu, X. Zhao, J. Zhou, R. Fang, F. Wang, Y. Li, Efficient Photoreduction of Diluted CO2 to Tunable Syngas by Ni−Co Dual Sites through d-band Center Manipulation, Angew. Chem. Int. Ed. 61 (2022) e202210576. https://doi.org/10.1002/anie.202210576.

11. K. Lu, Y. Li, F. Zhang, M. Qi, X. Chen, Z. Tang, Y.M.A. Yamada, M. Anpo, M. Conte, Y. Xu, Rationally designed transition metal hydroxide nanosheet arrays on graphene for artificial CO2 reduction, Nature Communications 11 (2020) 5181. https://doi.org/10.1038/s41467-020-18944-1.

12. Y. Su, Z. Song, W. Zhu, Q. Mu, X. Yuan, Y. Lian, H. Cheng, Z. Deng, M. Chen, W. Yin, Y. Peng, Visible-Light Photocatalytic CO2 Reduction Using Metal-Organic Framework Derived Ni(OH)2 Nanocages: A Synergy from Multiple Light Reflection, Static Charge Transfer, and Oxygen Vacancies, ACS Catal. 11 (2021) 345-354. https://doi.org/10.1021/acscatal.0c04020.

13. S. Bai, Z. Wang, L. Tan, G.I.N. Waterhouse, Y. Zhao, Y. Song, 600 nm Irradiation-Induced Efficient Photocatalytic CO2 Reduction by Ultrathin Layered Double Hydroxide Nanosheets, Ind Eng Chem Res 59 (2020) 5848-5857. https://doi.org/10.1021/acs.iecr.0c00522.

14. F. Chen, L. Zhou, C. Peng, D. Zhang, L. Li, D. Xue, Y. Yu, Bimetal-organic layer-derived ultrathin lateral heterojunction with continuous semi-coherent interfaces for boosting photocatalytic CO2 reduction, Applied Catalysis B: Environmental 331 (2023) 122689. https://doi.org/10.1016/j.apcatb.2023.122689.

15. W. Chen, B. Han, Y. Xie, S. Liang, H. Deng, Z. Lin, Ultrathin Co-Co LDHs nanosheets assembled vertically on MXene: 3D nanoarrays for boosted visible-light-driven CO2 reduction, Chem. Eng. J. 391 (2020) 123519. https://doi.org/10.1016/j.cej.2019.123519.